RAA 2015 Vol. **15** No. **11**, 1917–1930 doi: 10.1088/1674–4527/15/11/013
http://www.raa-journal.org *http://www.iop.org/journals/raa*

***R**esearch in*
***A**stronomy and*
***A**strophysics*

Antenna system characteristics and solar radio burst observations

Sha Li[1,2,3], Yi-Hua Yan[1,2], Zhi-Jun Chen[1,2], Wei Wang[1,2] and Dong-Hao Liu[1]

[1] Key Laboratory of Solar Activity, National Astronomical Observatories, Chinese Academy of Sciences, Beijing 100012, China; *lisha1400@bao.ac.cn*
[2] Key Laboratory of Radio Astronomy, Chinese Academy of Sciences, Beijing 100012, China
[3] University of Chinese Academy of Sciences, Beijing 100049, China

Received 2015 March 24; accepted 2015 April 28

Abstract The Chinese Spectral Radio Heliograph (CSRH) is an advanced aperture synthesis solar radio heliograph, independently developed by National Astronomical Observatories, Chinese Academy of Sciences. It consists of 100 reflector antennas, which are grouped into two antenna arrays (CSRH-I and CSRH-II) for low and high frequency bands respectively. The frequency band of CSRH-I is 0.4–2 GHz and that for CSRH-II is 2–15 GHz. In the antenna and feed system, CSRH uses eleven feeds to receive signals coming from the Sun. The radiation pattern has a lower side lobe and the back lobe of the feed is well illuminated. The characteristics of gain G and antenna noise temperature T affect the quality of solar radio imaging. For CSRH, the measured G is larger than 60 dBi and T is less than 120 K. After CSRH-I was established, we successfully captured a solar radio burst between 1.2–1.6 GHz on 2010 November 12 using this instrument and this event was confirmed through observations with the Solar Broadband Radio Spectrometer at 2.84 GHz and the Geostationary Operational Environmental Satellite. In addition, an image obtained from CSRH-I clearly revealed the profile of the solar radio burst. The other observational work involved the imaging the Fengyun-2E geosynchronous satellite which is assumed to be a point source. Results indicate that the data processing method applied in this study for deleting errors in a noisy image could be used for processing images from other sources.

Key words: techniques: image processing — techniques: interferometric — techniques: image processing

1 INTRODUCTION

In solar radio observations, the Sun exhibits a variety of large dynamic phenomena in different frequencies. At the same time, it radiates a relatively constant amount of energy toward the Earth (Takano 1996). These phenomena reveal the links between solar astronomy and other branches of physics. For example, solar observations can be well explained by magnetohydrodynamics (MHD) and plasma physics. The fundamental concept behind MHD shows that the magnetic field can induce currents in a moving conductive fluid, which creates forces on the fluid and also changes the magnetic field itself. The plasma is composed of ions and electrons and it is the key to understanding the propagation of radio waves coming from the Sun. CSRH observations with high spatial resolution can provide important diagnostic tools for understanding the behavior of the magnetic field, as well as solar radio density, plasma temperature, etc (Yan et al. 2009). Imaging spectroscopy over centimeter and decimeter wavelength ranges is important for CSRH to explain fundamental problems such as energy release, particle acceleration and particle transport.

In view of the available solar radio astronomical instruments all over the world, two main kinds of instruments are used in solar observations. One is the radio heliograph at single or discrete frequencies, for example, the Nançay Radio Heliograph (NRH) observes the Sun at 150, 164, 237, 327 and 410 MHz, the Nobeyama Radio Heliograph (NoRH) (Nakajima et al. 1994) observes the Sun at 17 and 34 GHz and the Siberian Solar Radio Telescope (SSRT) (Uralov et al. 1998) observes the Sun at 5.7 GHz (Lesovoi et al. 2014). Other instruments are spectrometers at certain frequency bands and frequency points, such as the Solar Broadband Radio Spectrometer (SBRS) at 1–2, 2.6–3.8, 5.2–7.6 and 2.84 GHz. Although scientists have developed some good theoretical models from observations with these instruments, there are still a lot of phenomena that cannot be explained by current observations and theories. So, a radio heliograph that can provide solar images in ultra wide band width is required. The ongoing operation of CSRH that can provide high temporal, spatial and spectral resolution will create radio images with ultra wide band width. These can be expected to provide better observations that can be used to explain solar phenomena (Chen et al. 2014).

The aim of CSRH is to provide a new tool for observing solar radio emissions, including radio bursts from primary energy release sites of solar energetic events such as flares and coronal mass ejections (CMEs). Solar flares generate a rich variety of solar radio bursts, which are believed to be due to the sudden process of energy release arising from topological reorganization in the solar magnetic field or through magnetic reconnection. CSRH will make full disk solar radio images with multiple frequency channels with a 25 ms cadence in its measurements.

There are errors in the radio heliograph, such as correlation-based errors, antenna pointing precision errors, and receiver output noise errors. Because there are so many sources of error, we have to calibrate the phase and amplitude errors of each output signal. The amplitude calibration is performed by comparing and equalizing the signal levels in the elements of an antenna array. By considering the instrument's errors, the measurement of phase calibration between different channels should make use of the celestial radio source from this theory, and the phase corrections are applied to the actual solar observations. As is well known, the sensitivity of a point source is proportional to the effective collecting area of the telescope, and this area is determined by one antenna making coordinated observations with a number of other antennas. In fact, the Sun is larger than the beam of individual antennas (Liu et al. 2007), so a number of pointing directions should be used.

To evaluate the CSRH antenna system, the gain and noise temperature of the antenna, and the sensitivity of the receiver should be measured. This paper presents a method for computing the characteristics of CSRH, and provides the results of the antenna gain G and antenna temperature T. This paper also gives two observational works. One is a solar radio burst observation and the other is satellite source imaging. The solar radio burst was observed by the CSRH-I 5-element array on 2010 December 12. This instance was also captured by SBRS at 2.84 GHz and Geostationary Operational Environmental Satellite (GOES) in X-ray. Another result came from observing the Fengyun-2E geosynchronous satellite at a height of nearly 35 600 km. The output signal from each antenna was calibrated by using this known standard satellite source as a reference. Then, we produced the images with Common Astronomy Software Application (CASA) which is an image layout software package used for aperture synthesis telescopes.

The content of this paper is arranged as follows. Section 2 gives a description of CSRH along with the measured and simulated radiation patterns. In Section 3, the antenna noise temperature and gain of the system are calculated in detail. Section 4 provides images of the solar radio burst and satellite point source, which are drawn by using calibrated data from CSRH. Finally, the conclusions are given in Section 5.

2 ANTENNA SYSTEM

2.1 About CSRH

CSRH is a radio interferometer which contains 100 parabolic reflector antennas. CSRH-I consists of 40 4.5-m-diameter antennas operating between 0.4–2 GHz and CSRH-II consists of 60 2-m-diameter antennas that observe from 2 to 15 GHz.

Figure 1 shows a photo of the constructed CSRH, which occupies 3.87 hectares and is located in Inner Mongolia, 400 km away from Beijing. The exact geographical coordinates of the central antenna are located at 115 degrees 15 minutes 1.8 seconds East longitude and 42 degrees 12 minutes 42.6 seconds North latitude. The antenna configuration (Yan et al. 2009) is a non-redundant array with good (u, v) coverage. The baseline vector has components (u, v, w), where w points in the direction of interest. u, v, w are measured in wavelengths at the center frequency of the radio frequency (RF) signal band, and in the directions towards East, North, and the phase tracking center respectively. For (u, v) coverage, if we assume the spatial frequencies are as follows

$$\boldsymbol{f}=(u, v)\,, \tag{1}$$

these are the conjugate coordinates of the spatial coordinates (x, y) in the image plane. Also, (x, y) measure angles, which are usually expressed in arcseconds, and spatial frequencies measure distance in the incident wavefront measured in wavelength units, which are usually expressed in arcsec^{-1}, as shown in Equation (2),

$$\boldsymbol{f} = (u, v) = \frac{1}{\lambda}(\Delta X, \Delta Y)\,. \tag{2}$$

During the imaging process, the incoming wavefront is spatially sampled by the radio heliograph, and we need to make our measurements in a plane which are measured in terms of wavelength. When we observe the Sun, the sampling of the incident wavefront is no longer continuous and depends on the array configuration. The Fourier components of the object are measured at different spatial frequencies.

Figure 2 shows the arrangement of CSRH-I. Figure 3 gives the (u, v) coverage (Millard & Howell 2008) of Figure 2. All the antennas are arranged in three spiral arms (named the A axis, B axis and C axis respectively).

For multiple-element antenna arrays, it is convenient to specify the antenna positions relative to the reference point measured in a Cartesian coordinate system, a system with axes pointing towards hour-angle h and declination δ equal to ($h = 0$, $\delta = 0$) for X, ($h = -6^h$, $\delta = 0$) for Y, and ($\delta = 90\,\mathrm{deg}$) for Z. If we assume L_X, L_Y and L_Z are the corresponding coordinate differences for two antennas, the baseline components (u, v, w) are given by Equation (3)

$$\begin{pmatrix} u \\ v \\ w \end{pmatrix} = \frac{1}{\lambda} \begin{pmatrix} \sin H_0 & \sin H_0 & 0 \\ -\sin\delta_0 \cos H_0 & \sin\delta_0 \sin H_0 & \cos\delta_0 \\ \cos\delta_0 \cos H_0 & -\cos\delta_0 \sin H_0 & \sin\delta_0 \end{pmatrix} \begin{pmatrix} L_X \\ L_Y \\ L_Z \end{pmatrix}\,, \tag{3}$$

where H_0 and δ_0 are the hour-angle and declination of the phase reference position, and λ is the wavelength corresponding to the center frequency of the receiving system. The elements in the transformation matrix in Equation (3) are the direction cosines of the (u, v, w) axis relative to (X, Y, Z) axes. Thus as the interferometer observes a point source on the celestial sphere, the rotation of the Earth causes the u and v components of the baseline to trace out an elliptical locus. This ellipse is simply the projection onto the (u, v) plane of the circular locus traced out by the tip of the baseline vector, and at any instant the correlator output provides a measure of the visibility at two points in the (u, v) plane. For an East-West baseline $L_Z = 0$, and a single ellipse is centered on the origin of the (u, v) system.

Fig. 1 A view of CSRH.

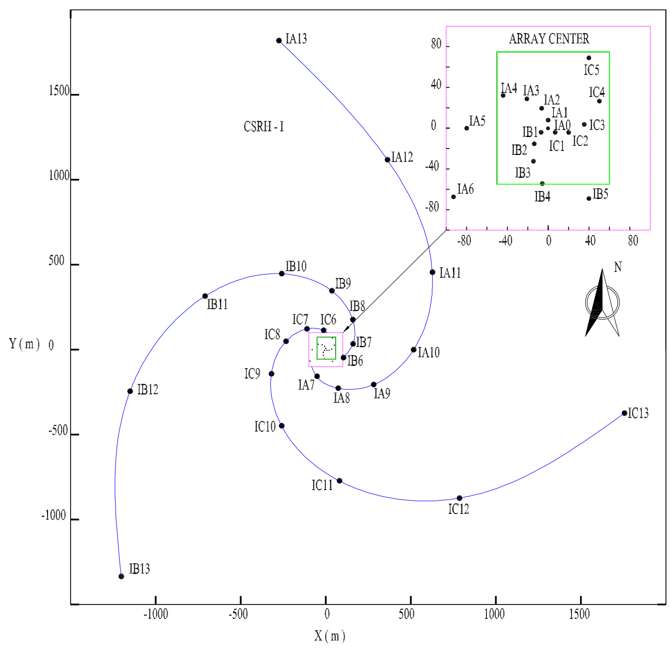

Fig. 2 The 2D configuration of CSRH-I. The antennas are arranged in three spiral arms (named the A axis, B axis and C axis respectively). Every axis has 13 antennas and IA0 is in the center of the antenna array. Its corresponding coordinate is (0,0)m and the locations of other antennas are referenced with respect to antenna IA0. The black filled circles are the locations of each antenna.

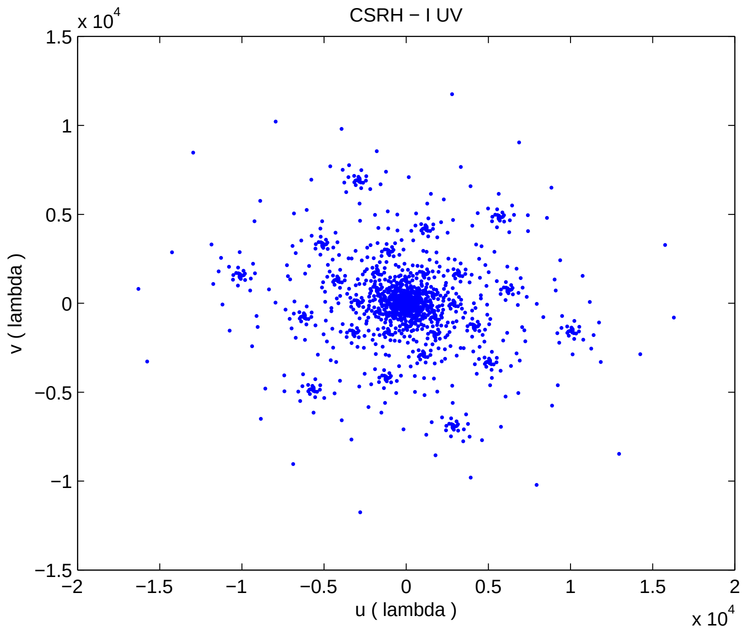

Fig. 3 (u, v) coverage of CSRH-I. The blue points correspond to the locations of each (u, v) coverage of the source image. The number of baselines is 780 for this radio heliograph. A stellar interferometer only measures one visibility per baseline.

Table 1 CSRH-I Characteristics and Specifications

Observing band	0.4–2 GHz
Spatial Resolution	51.6″–10.3″
Temporal Resolution	100 ms
Dynamic range of images	$\geq$ (25 dB)
Polarization	left and right circular polarization
Frequency channel	64
Observing period	0 UT to 8 UT in winter, –1 UT to 9 UT in summer
Antenna efficiency	$\geq (0.4)$
Antenna noise temperature	$\leq$(120 K)

The characteristics and specifications of CSRH-I are shown in Table 1. This array has 64 frequency channels and 16 channels per sub-band. The detailed specifications of CSRH-II will be introduced in a future paper.

To cover a wide frequency range with high sensitivity, the bandwidth of CSRH-I is divided into four sub-bands: 0.4–0.8, 0.8–1.2, 1.2–1.6 and 1.6–2.0 GHz. When the RF signal from the Sun arrives at the analog receiver of CSRH, it is mixed with two local oscillators. The first oscillator mixes the four sub-bands at 3.6, 4.0, 4.4 and 4.8 GHz respectively. So, all four sub-bands become 2.8–3.2 GHz after applying the first oscillator. Then, the output of the first oscillator is further mixed with the second oscillator at a frequency of 3.25 GHz. Thus, the output frequencies of all four sub-bands range from 50 MHz to 450 MHz.

In CSRH-I, to ensure all RF signals arrive simultaneously, the optical fibers that transmit the received RF signals from all channels have the same length. Each pair of antennas is correlated to output a Fourier component of a solar radio image. Then we can reconstruct the brightness image through gathering all possible Fourier components by employing interferometry.

2.2 Simulation of the Radiation Pattern for the Feed and Reflector Antenna System

CSRH is an ultra wide band radio heliograph. Regarding how to choose a feed that can be used in CSRH, there are many kinds of ultra wide band feeds (Taylor et al. 1999) in different antenna systems, but some have shortcomings. For example, a ridged horn is too heavy and expensive; a log-periodic antenna has a variable phase center location and it spills over the edge of the dish to reduce the gain of the antenna system. In addition, the 3 dB beamwidth of the radiation patterns of these two feeds is not wide enough, so the reflector surface cannot be fully illuminated by the feed, which will result in inefficient usage of the reflector antenna. For CSRH, we use eleven feeds to receive radio signals because this design has many advantages, such as a fixed phase center location, well-shaped radiation patterns and low return loss. This feed is comprised of 13 folded dipoles. The bandwidth is decided by the ratio of the length of the "next-to-shortest" dipole to the length of the "next-to-longest" dipole. "Next-to-shortest" means the shorter dipole of the two adjacent dipoles and "next-to-longest" means the longer dipole of the two adjacent dipoles. The length of the longest dipole is given by the wavelength of the lowest frequency. Figure 4 shows a photo of the CSRH-I feed.

In the simulation stage, we use High Frequency Structure Simulator (HFSS) software to simulate the radiation pattern of the feed and reflector antenna system of CSRH. In order to get a good radiation pattern, dipoles at different heights vary sequentially (Qing & Chia 1999) according to the optimized scaling ratio. Then, the derived radiation pattern of the feed is substituted into the feed and reflector antenna model, and we can obtain the radiation pattern of the whole system.

Figures 5, 6 and 7 show the simulated 3D radiation patterns of the feed and reflector antenna system at 0.4, 1.2 and 2 GHz respectively. The feed is located at the focus of the parabolic reflector antenna, and the pattern is symmetric about the z-axis. We can see that the radiation patterns are symmetric with respect to the boresight.

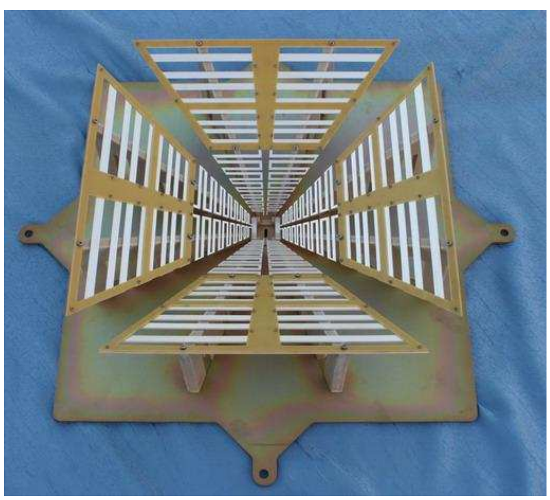

Fig. 4 A photo of the CSRH-I feed.

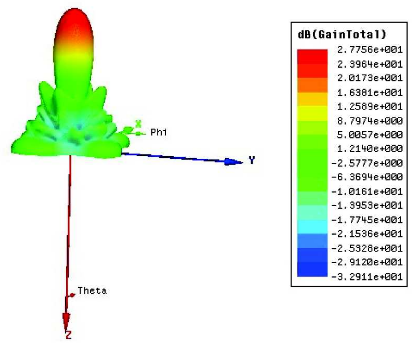

Fig. 5 Simulated 3D radiation pattern of the feed and reflector antenna at 0.4 GHz. The right scale shows different colors corresponding to different values of total gain in dB.

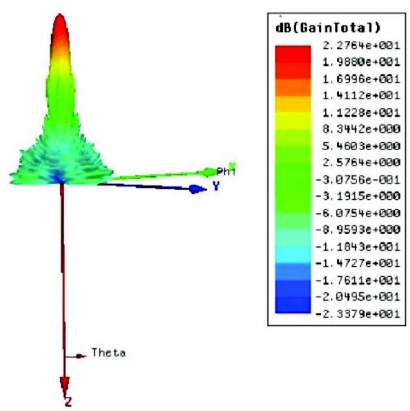

Fig. 6 Simulated 3D radiation pattern of feed and reflector antenna at 1.2 GHz. The right scale shows different colors corresponding to different values of total gain in dB.

To check the consistency between the simulated and measured radiation patterns, we observed the Fengyun-2E satellite at 1.7 GHz. This satellite beacon signal was received by antenna IA0. The antenna moved in the up and down directions and in the left and right directions, so the measured radiation patterns in the elevation and azimuth directions were obtained independently by receiving signals from the maximum satellite downlink signal. The simulated and measured radiation patterns are illustrated at 1.7 GHz in Figure 8.

In the antenna system, the parameter G is measured using two antennas (IB11 and IA0). IB11 was connected to a signal source, and it transmitted a signal to IA0. IA0 received the signal from the source and the spectrum analyzer was connected to IA0. The ratio of the powers from the signal source and from the spectrum analyzer could be obtained, so we could measure the antenna gain G from Equation (4).

$$G = \frac{(27000 \sim 31000)}{\theta_{\text{azimuth}}\theta_{\text{elevation}}}\,, \tag{4}$$

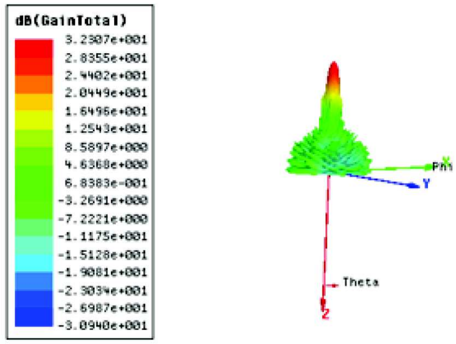

Fig. 7 Simulated 3D radiation pattern of feed and reflector antenna at 2 GHz. The left scale shows different colors corresponding to different values of total gain in dB.

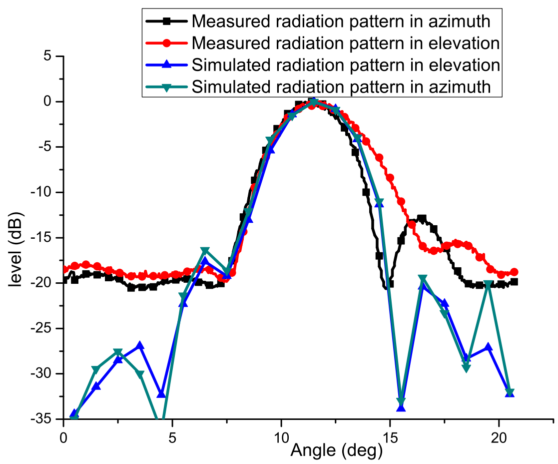

Fig. 8 Simulated and measured 2D radiation patterns in 1.7 GHz. The black line with squares and red line with circles represent the radiation pattern in the elevation and azimuth directions respectively; the blue line with upward triangles and the dark cyan line with downward triangles represent radiation pattern in elevation direction and azimuth directions respectively.

where θ_{azimuth} and $\theta_{\text{elevation}}$ are the 3 dB beamwidths in the azimuth and elevation directions respectively (Kildal 2009). The directivity coefficient D is calculated by Equation (5).

$$D = \left(\frac{\pi d}{\lambda}\right)^2, \tag{5}$$

where d and λ represent the diameter of the reflector antenna and the wavelength of the working frequency. From Equations (4) and (5), the measured G and calculated D are 34.61 dB and 38.08 dB respectively. Thus, the relationship between G, D and antenna efficiency η is expressed in Equation (6)

$$G = D \times \eta\,. \tag{6}$$

We calculated η to be 0.45 which satisfies the specification of this antenna design.

2.3 The Equatorial Mount and Pointing Error of the Reflector Antenna of CSRH

To facilitate the observation of the Sun, the reflector antenna of CSRH is designed with an equatorial mount (also called a polar mount) and uses a quadrupod structure to support the feed. The foot points of this quadrupod are located at the edge of the reflector antenna to reduce their influence on the incoming plane wave. The equatorial mount follows the rotation of the sky (celestial sphere) by having one rotational axis parallel to the Earth's axis of rotation. In addition, it makes all the antennas operate consistently. The monitoring subsystem sends the control signal to the operating unit of an antenna, and the antenna reacts to the signal by adjusting its position to work in an optimal way.

The pointing error of each antenna is very important for an extended source such as the quiet Sun. If the pointing error of the antenna is not accurate, it would influence the phase correlation, which could not be deleted by post-processing. The measured pointing error of each antenna in CSRH is less than $9'$. When all the antennas point to the Sun after calibration, the response of the receivers must be uniform over the whole angular range of the observation.

3 ANTENNA NOISE TEMPERATURE

3.1 Theoretical Analysis of Antenna Noise Temperature

In the CSRH program, it is necessary to choose an appropriate amplifier (Kildal 2009) that matches the antenna system. The antenna and receiver system noise temperature must be lower than the specification of the whole system.

The classical method of measuring antenna noise temperature is based on separating the detection of an astronomical source from the sky background. These measurements could be extended for judging the system independent of the telescope antenna. Signals coming from the sky background noise and astronomical source need to be measured at frequencies supported by the antenna-feed. When solar radio observation is required, the antenna noise temperature (Kildal & Sipus 1995) is measured in the whole system. This relies on the reflector configuration and the feed radiation pattern, which means that if the feed has a low sidelobe and cross polarization (Olsson et al. 2006), the reflection from the ground plane will be reduced. At the same time, it could minimize the spillover from the sidelobes and the selection of feed is vital to the whole antenna system.

When observing solar radio signals, circular polarization (Uralov et al. 1998) has been demonstrated by studies of large numbers of solar storms. The characteristic of the wave is effected by antenna gain, effective aperture, antenna noise temperature and so on. The reduction in the system noise temperature could improve the sensitivity of a radio telescope (Li et al. 2015). Minimizing radio noise temperature usually involves cooling the amplifier from the front end of the system. It is convenient to use cosmic sources with small angular size as a calibrated source, because the flux density of these sources is already known. However for the Sun, it is impossible to use a cosmic source because the Sun is stronger than any other source. Thus, a noise source that acts as a standard source is mounted in the input port of the analog system. The input port is connected to the load, the antenna observation of sky background and the standard noise generator, and the output data are gathered to compute antenna noise temperature. The thermal noise source used in this measurement is the resistor which is connected to the receiver by coaxial lines. The noise temperature of the receiver and antenna system is measured by the Y factor method. The factor Y is represented by

$$Y = 10^{(P1-P2)/10}\,, \tag{7}$$

where $P1$ and $P2$ correspond to the powers of different loads added at the end of the system. After obtaining Y, the antenna noise temperature $T_{\rm A}$ is computed by

$$T_{\rm A} = (T_0 + T_{\rm r} - Y \times T_{\rm r})/Y\,, \tag{8}$$

where T_0 represents the ambient temperature, $T_0 = 290$ K, and T_r means the temperature of the analog receiver.

The noise temperature of the whole system is the sum of the antenna system noise temperature and the receiver noise temperature. Equations (9), (10) and (11) show different received powers with different loads. In these equations, $k = 1.3806505 \times 10^{-23}$ J K^{-1}, B represents the bandwidth, and G_r is the gain of the system coming from the noise source of the receiving system. The noise temperature T_NS means noise associated with the terminal that is connected to the noise source, $T_{50} = 290$ K, and the noise temperature T_{50} means noise associated with the terminal that is connected with standard impedance 50 Ω.

$$[(T_{50} + T_\mathrm{r})\, kB] + [G_\mathrm{r}] = [P_{50}]\,, \tag{9}$$

$$[(T_\mathrm{NS} + T_\mathrm{r})\, kB] + [G_\mathrm{r}] = [P_\mathrm{NS}]\ , \tag{10}$$

$$[(T_\mathrm{A} + T_\mathrm{r})\, kB] + [G_\mathrm{r}] = [P_\mathrm{SKY}]\ . \tag{11}$$

The square brackets in Equations (9), (10) and (11) mean that the unit of each value is dB. From Equations (12), (13) and (14), we could get the representations of T_r, G_r and T_A respectively.

$$T_\mathrm{r} = \frac{T_\mathrm{NS} - T_{50}\left(\frac{P_\mathrm{NS}}{P_{50}}\right)}{\frac{P_\mathrm{NS}}{P_{50}} - 1}, \tag{12}$$

$$G_\mathrm{r} = \frac{P_{50}\left(\frac{P_\mathrm{NS}}{P_{50}} - 1\right)}{kB\,(T_\mathrm{NS} - T_{50})}, \tag{13}$$

$$T_\mathrm{A} = \frac{P_\mathrm{SKY}}{P_{50}}(T_{50} + T_\mathrm{r}) - T_\mathrm{r}. \tag{14}$$

3.2 The Measured Results of CSRH

For the CSRH radio heliograph, we test the gain by using the Y factor method (Penzias & Wilson 1965) in the whole system. Table 2 gives the measured noise temperatures of the noise source at different frequencies. The relationship between Excess Noise Ratio (ENR) and the noise source temperature is

$$\mathrm{ENR} = \frac{T_\mathrm{NS} - T_0}{T_0}, \tag{15}$$

where T_0 is the ambient temperature, here $T_0 = 290$ K. From Table 2, it can be observed that the noise temperature decreases as the frequency increases.

Table 2 The noise temperatures (T_NS) of the noise source at different frequencies. From instrumental measurements, ENR means the multiple of the noise source above the ambient temperature.

Radio frequency (GHz)	ENR (dB)	Noise temperature (K)
0.75	21.28	392230.18
0.8	21.03	37051.90
1.025	20.57	33357.24
1.2	20.18	30517.21
1.45	19.82	28112.62
1.95	18.71	21837.56

Table 3 lists the noise powers of different terminals: noise source, 50 Ω impedance, sky background and the Sun. Based on the measured results of Table 3, we can calculate system noise ($T_{\rm r}$), system gain ($G_{\rm r}$) and antenna noise temperature ($T_{\rm A}$) by using Equations (12), (13) and (14) respectively. The calculated results are shown in Table 4. The fourth column of this table gives values for the measured antenna noise temperature. They are all less than the specification 120 K at different frequencies.

Table 3 The values for the noise power of different terminals including the noise generator, 50 Ω impedance, sky background and the Sun at different frequencies ($P_{\rm NS}$, P_{50}, $P_{\rm SKY}$, and $P_{\rm sun}$ represent the measured powers of the terminals).

Radio frequency (GHz) (1)	$P_{\rm NS}$ (dBm) (2)	P_{50} (dBm) (3)	$P_{\rm SKY}$ (dBm) (4)	$P_{\rm sun}$ (dBm) (5)
0.75	–26.19	–44.93	–46.58	–39.25
0.8	–24.98	–42.81	–44.42	–37.83
1.025	–22.21	–40.52	–42.78	–35.65
1.2	–28.31	–44.6	–46.36	–41.5
1.45	–29.81	–46.80	–48.57	–42.13
1.95	–28.86	–43.61	–45.2	–41.5

Table 4 The measured system noise ($T_{\rm r}$), system gain ($G_{\rm r}$) and antenna noise temperature ($T_{\rm A}$) at different frequencies.

Radio frequency (GHz) (1)	$T_{\rm r}$ (K) (2)	$G_{\rm r}$ (dB) (3)	$T_{\rm A}$ (K) (4)
0.75	268.3	61.7	92.9
0.8	326.05	63.12	99
1.025	235.7	66.4	58.9
1.2	437.3	60.61	48
1.45	308.3	59.9	69.8
1.95	456.42	61.49	61.17

4 DATA PROCESSING FOR CSRH-I

4.1 Solar Radio Burst Observation

An example of a solar radio burst is provided to validate the effectiveness of observations made by CSRH. This event occurred on 2010 November 12. By using a 5-element system of that is part of CSRH-I, we successfully observed a solar radio burst that was associated with a C1.5 class X-ray flare. In the Huairou observing station, SBRS also observed this event at the same time. In addition, GOES observed this event in X-ray at that time.

Figure 9(a) gives the observed fringe acquired with the IB7-IC1 baseline, where IB7 and IC1 are two antennas that are part of CSRH-I. The black curve shows the amplitude of the Fourier component, and the red and blue curves show the cosine and sine components respectively; Figure 9(b) gives the flux density provided by GOES at a wavelength of 1–8 Å represented by a black line and 0.5–4 Å drawn in a red line; Figure 9(c) shows the total flux density measured by the instrument at Huairou observing station and the results observed by antenna IC1.

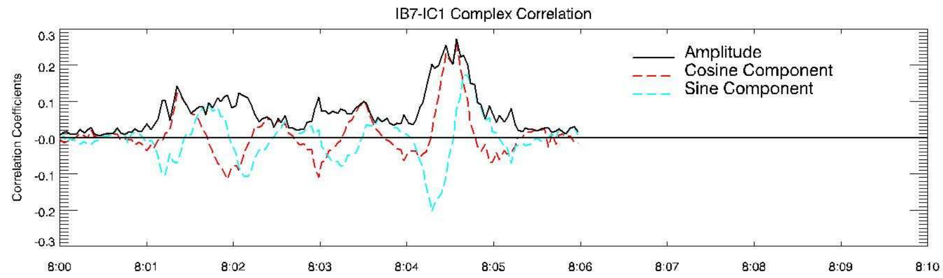

(a)

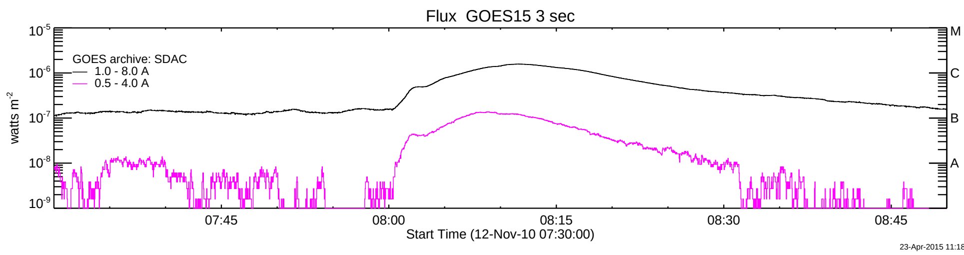

(b)

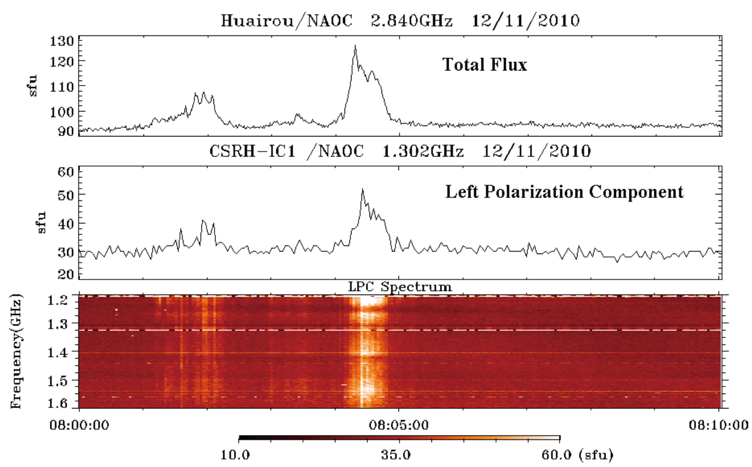

(c)

Fig. 9 A comparison between observations made by different instruments. (a) The observed fringe includes the sine and cosine components; (b) The flux density observed by GOES; (c) The measured result obtained by IC1.

4.2 Satellite Image Using the Aperture Synthesis Method

Regarding the CSRH-I image calibration, the diameter of the antenna is too small to use non-solar compact sources as a calibrated source. Therefore, we used the beacon signal from the Fengyun-2E satellite as a point source at the beginning stage of testing CSRH at 1.7 GHz.

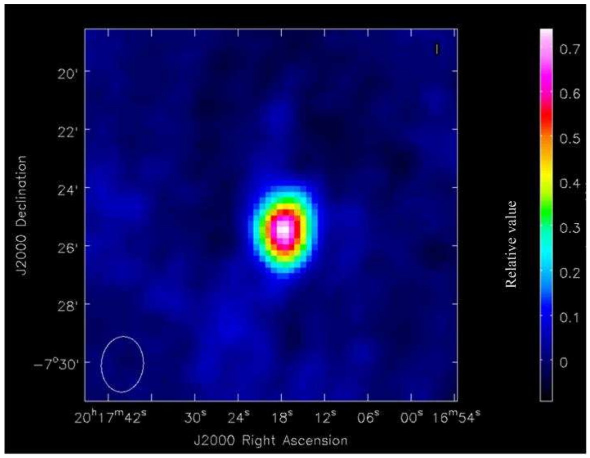

Fig. 10 Stokes parameter I: the cleaned observed image of the Fengyun-2E satellite at 1.7 GHz on 2013 June 4th. The ellipse in the lower left corner is the synthesized beam and the vertical scale bar represents the relative level of the background.

The result of observing Fengyun-2E is drawn in Figure 10. There are a total of 930 Fourier components using 31 antennas, and each pair of these antennas is used in interferometry to provide a Fourier component of the observed source. The brightness image of the observed source can be obtained (Wang et al. 2013) through applying an inverse Fourier transform to the gathered Fourier components.

For detecting the satellite source, an observation is obtained during the pass of the source through a stationary beam. Figure 10 shows the Stokes parameter I, which represents the total intensity of the satellite source. The phase error of spherical waves coming from the satellite would be more than $360°$ for the long baseline, and varies with the motion of the satellite. However, such an error could be successfully removed using two observations. Figure 10 is obtained from CASA. The integration time is 30 ms and the beam size of this image corresponding to the antenna beam is $1.25' \times 2.489'$. This observation demonstrates the good performance of the imaging capability of CSRH-I.

5 CONCLUSIONS

The characteristics of CSRH are presented in this paper. From these data, we found that the system gain G_r is larger than 60 dBi and the antenna noise temperature T_A is less than 120 K, which satisfy the specifications of our science requirement. After some of the antennas were installed in Mingantu Observing Station, a solar radio burst at 1.302 GHz was successfully captured by five elements that are part of CSRH, on 2010 November 12 at the same time that SBRS and GOES also observed this event. Another result comes from the point source observation of a satellite image at 1.7 GHz, which demonstrates the imaging ability of this system. CSRH will acquire solar radio images in decimeter and centimeter wavelengths more accurately.

Acknowledgements We acknowledge the anonymous referee for his/her valuable suggestions and comments on this paper. The authors also wish to thank Long Xu, Chong Huang, Cheng Ming Tan and Jing Huang for their generous advice on this paper. This work is supported by National Basic Research Program of China (973 program, MOST2011CB811401), the National Natural Science Foundation of China (Grant Nos. 11221063, 10778605, 11003028, 11203042, and U1231205), and the National Major Scientific Equipment Research and Design project (ZDYZ2009-3).

References

Chen, J.-J., Bai, Z.-R., Luo, A.-L., & Zhao, Y.-H. 2014, in Society of Photo-Optical Instrumentation Engineers (SPIE) Conference Series, 9149, 1

Kildal, P. S. 2009, Foundations of Antennas (Chalmers: Chalmers University of Technology), 44

Kildal, P., & Sipus, Z. 1995, IEEE Antennas and Propagation Magazine, 37, 114

Lesovoi, S. V., Altyntsev, A. T., Ivanov, E. F., & Gubin, A. V. 2014, RAA (Research in Astronomy and Astrophysics), 14, 864

Li, S., Yan, Y. H., Chen, Z. J., Wang, W., & Zhang, F. S. 2015, PASA, 32, 13

Liu, Z., Gary, D. E., Nita, G. M., White, S. M., & Hurford, G. J. 2007, PASP, 119, 303

Millard, L. D., & Howell, K. C. 2008, Journal of the Astronautical Sciences, 56, 71

Nakajima, H., Nishio, M., Enome, S., et al. 1994, Proceedings of the IEEE, 82, 705

Olsson, R., Kildal, P.-S., & Weinreb, S. 2006, IEEE Transactions on Antennas and Propagation, 54, 368

Penzias, A. A., & Wilson, R. W. 1965, ApJ, 142, 1149

Qing, X. M., & Chia, Y. W. M. 1999, Electronics Letters, 35, 2154

Takano, T. 1996, Magnetodynamic Phenomena in the Solar Atmosphere (Springer Netherlands), 569, *http://link.springer.com/chapter/10.1007/978-94-009-0315-9_143*

Taylor, G. B., Carilli, C. L., & Perley, R. A., eds. 1999, Astronomical Society of the Pacific Conference Series, 180, Synthesis Imaging in Radio Astronomy II

Uralov, A. M., Grechnev, V. V., Lesovoi, S. V., et al. 1998, Sol. Phys., 178, 119

Wang, W., Yan, Y., Liu, D., et al. 2013, PASJ, 65, 18

Yan, Y., Zhang, J., Wang, W., et al. 2009, Earth, Moon, and Planets, 104, 97